ACS Sustainable Chemistry & Engineering

Research Article

pubs.acs.org/journal/ascecg

Chemically Integrated Multiwalled Carbon Nanotubes/Zinc Manganate Nanocrystals as Ultralong-Life Anode Materials for Lithium-Ion Batteries

Wei Yao,* Jianguang Xu, Jia Wang, Juhua Luo, Qingle Shi, and Qi Zhang

School of Materials Engineering, Yancheng Institute of Technology, 211 East Jianjun Road, Yancheng, Jiangsu 224051, People's Republic of China

Supporting Information

ABSTRACT: Hybrid nanostructures based on carbon nanotubes and mixed transition-metal oxides hold a great promise as high-performance electrode materials for next-generation lithium-ion batteries. In this work, we report the synthesis of chemically integrated MWCNT/$ZnMn_2O_4$ (MZMO) hybrids via a polyol method and subsequent thermal annealing treatment. Benefiting from the larger specific surface area, strongly coupled interaction and synergic effect between $ZnMn_2O_4$ nanocrystals and MWCNT, the MZMO hybrids exhibit improved electrochemical performance, with a high reversible specific capacity, and excellent rate capability, as well as a superior cycle stability. After 100 cycles, the MZMO2 demonstrates a reversible capacity of 847 mA h g^{-1} at a current density of 400 mA g^{-1}. Even at 1600 mA g^{-1} up to 1000 cycles, the reversible capacity still preserves 527 mAh g^{-1}, which is much higher than the theoretical capacity of graphite.

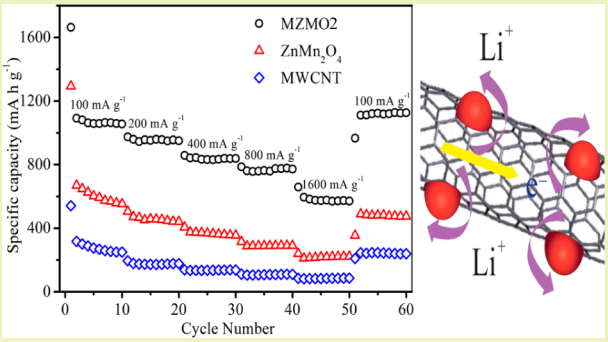

KEYWORDS: *Zinc manganate, Multiwalled carbon nanotubes, Anode materials, Synergic effect, Li-ion battery*

INTRODUCTION

Lithium-ion batteries (LIBs), as one of the extremely important storage devices, have broad applications in portable electronic devices, electric vehicles and hybrid electric vehicles.[1−4] With the increasing market demands for LIBs, great researches have paid attention to the exploration of advanced anode materials with high specific capacity and long-life cycling stability.[5,6] Because of their higher theoretical capacity (500−1000 mA h g^{-1}), transition-metal oxides (TMOs), such as Co_3O_4,[7] MnO,[8] Fe_2O_3[9] and SnO_2,[10] have been intensively investigated as LIBs anode materials for replacing graphite, the capacity of which is only 372 mA h g^{-1}.[11] Unfortunately, these single metal oxides undergo large volume changes during the charging and discharging processes, leading to the deterioration of capacity and rate capability.[12,13]

It is interesting to note that mixed transition-metal oxides (MTMOs) in spinel structure, such as AB_2O_4 ($ZnCo_2O_4$,[12−14] $NiCo_2O_4$,[15] $ZnMn_2O_4$,[16] $ZnFe_2O_4$,[17,18] etc.), have exhibited good electrochemical properties as anode materials owing to their higher electrical conductivity and lager specific capacity than that of TMOs. Among above anode materials, $ZnMn_2O_4$ has attracted much attention on account of its low cost, resource abundance, environmental friendliness, and much lower operating voltage compared with Co- or Fe-based oxides.[19−21] $ZnMn_2O_4$ could store Li^+ through not only the conversion reaction 1, 2 and 3 but also the alloying/dealloying reaction 4 between Zn and Li, leading to a high theoretical specific capacity of 1024 mAh g^{-1}.[22]

$$ZnMn_2O_4 + 8Li^+ + 8e^- \rightarrow Zn + 2Mn + 4Li_2O \quad (1)$$

$$Zn + Li_2O \rightarrow ZnO + 2Li^+ + 2e^- \quad (2)$$

$$Mn + Li_2O \rightarrow MnO + 2Li^+ + 2e^- \quad (3)$$

$$Zn + Li^+ + e^- \rightarrow LiZn \quad (4)$$

Up to now, $ZnMn_2O_4$ nanomaterials in different morphologies, such as nanoparticles,[16,23−25] nanocrystalline,[26,27] nano/microspheres,[22,28−31] nanorods/nanowires/nanotubes,[19,20,32] have been explored for LIBs, because anode materials in nanoscale can effectively shorten the reaction pathway of Li ions. However, the specific capacity, cycle stability and rate capability of $ZnMn_2O_4$ nanomaterials are still limited owing to the low electronic/ionic conductivity and detrimental structural collapse during the lithiation and delithiation processes.[33]

To solve these problems, one appealing strategy is to adopt a flexible matrix to alleviate the structure change and increase the electric conductivity of anode materials at the same time.[34,35] In this regard, graphene and carbon nanotubes (CNT) would be superior substrates to accommodate $ZnMn_2O_4$ in advanced

Received: May 15, 2015
Revised: August 1, 2015
Published: August 3, 2015

DOI: 10.1021/acssuschemeng.5b00434
ACS Sustainable Chem. Eng. 2015, 3, 2170−2177

anode materials, due to their excellent electrical conductivity, large surface area, high mechanical strength, and structural flexibility.[36,37] To date, graphene-wrapped $ZnMn_2O_4$[38] and $ZnMn_2O_4$ nanosheets@carbon nanotubes[33] have been prepared by electrostatic adsorption strategy and in situ growth method, respectively. Nevertheless, on account of the weak interaction between carbon (graphene or CNT) and $ZnMn_2O_4$, the cycle number of nanocomposites is only 50−100 and still needs to be improved. Recent research shows that strongly coupled interaction between graphene and $ZnMn_2O_4$ can restrain the structure collapse of hybrids, resulting in ultralong life up to 1500 cycles.[38] However, the existence of defects and oxygenic groups on graphene sheets decreases its electrical conductivity and limit the lithium storage properties of the hybrid material. It is postulated that multiwalled carbon nanotubes (MWCNT) could overcome above problems as the outer wall can be mildly oxidized by a modified Hummers method to integrate chemically with metal oxides, whereas the inner graphitic walls provide excellent conductivity.[40,41] Therefore, through strongly coupled interaction, hybrid nanostructure of MWCNT supporting $ZnMn_2O_4$ is expected to achieve further optimization of lithium storage capability.

In this work, we present a two-step method to grow $ZnMn_2O_4$ nanocrystals on MWCNT (denoted as MZMO) via a polyol process followed by thermal annealing treatment. Because of the chemically integrated interaction between MWCNT and $ZnMn_2O_4$ nanocrystals, as well as the superior conductivity of MWCNT, the resulted MZMO2 anode material exhibits excellent lithium storage properties with a high specific capacity of 847 mA h g^{-1} after 100 cycles at a current density of 400 mA g^{-1}, as well as excellent rate capability and ultralong life up to 1000 cycles, all of which render it a superior anode material for high performance LIBs.

EXPERIMENTAL SECTION

Synthesis of MWCNT/$ZnMn_2O_4$ Nanocrystals (MZMO). The mildly oxidized carbon nanotubes (moMWCNT) were prepared by a modified Hummers method.[42] For the synthesis of MZMO, 24 mg of moMWCNT was added into 60 mL of ethylene glycol containing different content of $Zn(Ac)_2{\cdot}2H_2O$ (0.2, 0.4, 0.8 mmol, respectively) and $Mn(Ac)_2{\cdot}4H_2O$ according to a molar ratio of 1:2. After ultrasonic treatment for 2 h, the obtained dispersions were kept at 170 °C with stirring for 2 h. The precipitates were collected by centrifugation and washed with distilled water and ethanol three times. To obtain different ratios of MWCNT/$ZnMn_2O_4$ nanocrystals (noted as MZMO1, MZMO2 and MZMO3 with the content of $Zn(Ac)_2{\cdot}2H_2O$ from 0.2 to 0.8 mmol), the precipitates were annealed at 300 °C for 2 h in air with a slow heating rate of 1 °C min^{-1}. The $ZnMn_2O_4$ was prepared by the same method without the moMWCNT.

Characterizations. The morphologies of the samples were observed by field emission scanning electron microscopy (FESEM, Hitachi, S4800, Japan) with an accelerating voltage of 5 kV. The fine structures were characterized using transmission electron microscopy (TEM, JEOL, JEM-2100, Japan) and scanning transmission electron microscopy (STEM, FEI, Tecnai G2 F30 S-TWIN, America). The phase structure was identified by X-ray diffraction analysis (XRD, Rigaku, D/MAX2500 V, Japan) with Cu Kα radiation (λ = 1.5418 Å) at room temperature in the 2θ range of 10° to 70°. X-ray photoelectron spectrum (XPS, ESCALB MK-II, VG Co., England) was recorded under a base pressure of 1 × 10^{-9} Torr using monochromatic Mg Kα X-rays at hυ = 1253.6 eV. ATR-IR spectra were recorded on a Bruker Tensor 37 in the region of 4000−600 cm^{-1} by attenuated total reflection (ATR). Thermogravimetric analysis (TGA) was run on a Pyris1 TGA instrument from room temperature to 700 °C at a heating rate of 10 °C min^{-1} under air. Brunauer−Emmett−Teller (BET) measurements were carried out to determine the surface area of samples. Nitrogen sorption measurements of the dried samples that had been degassed at 120 °C under vacuum were performed on a Micromeritics ASAP 2020 analyzer.

Electrochemical Measurements. The working electrodes were prepared from the mixture containing 70 wt % active material, 20 wt % acetylene black, and 10 wt % polyvinylidene fluoride binder dissolved in *N*-methyl-2-pyrrolidinone. The average mass loading of all electrodes was about 0.8−1 mg cm^{-2}. Lithium metal was used as the counter electrode and reference electrode. The electrolyte was 1 M $LiPF_6$ in a 1:1 mixture (by volume) of EC/DMC with 2% vinylene carbonate. Cell assembly was carried out in an Ar-filled glovebox (Innovative Technology Inc.) with moisture and oxygen concentrations below 1.0 ppm. The galvanostatic charging/discharging measurements were conducted in the voltage range of 0.01−3.0 V on a NEWARE battery tester. Cyclic voltammetry (CV) measurements were carried out on a CHI660D electrochemical workstation (Shanghai CH Instrument Company, China) between 0.01 and 3.0 V at a scan rate of 0.1 mV s^{-1}. Electrochemical impedance spectroscopy (EIS) experiments were performed on an electrochemical workstation (ZAHNER ZENNIUM) in the range from 10 mHz to 100 kHz.

RESULTS AND DISCUSSION

Figure 1 schematically depicts the entire procedure for preparing MZMO. moMWCNT are first oxidized by a modified Hummers method,[42] to introduce oxygen functional groups (hydroxyl and carboxy groups) on the side walls of MWCNT (Supporting Information, Figure S1). In the following step, the moMWCNT are dispersed into ethylene glycol solution containing $Zn(Ac)_2{\cdot}2H_2O$ and $Mn(Ac)_2{\cdot}4H_2O$ with a stoichiometric ration of 1:2. Subsequently, the ZnMn−glycolate will be formed with preferred nucleation sites on the surface of moMWCNT at 170 °C through the strongly coupled effect between abundant functional groups on moMWCNT and metal ions.[39−41] Finally, the chemically integrated MZMO could be obtained by annealing treatment.

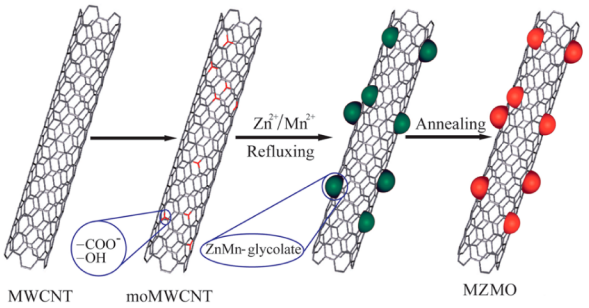

Figure 1. Schematic diagram of the synthetic route to the MZMO.

Figure 2 shows the typical TEM images of MWCNT and MZMO2. Similar to the MWCNT (Figure 2a), the MZMO2 demonstrates 1D microsized nanotube strucutures with a rough surface derived from $ZnMn_2O_4$ nanocrystals grafted on the surface of MWCNT (Figure 2b,c). The average particle size of $ZnMn_2O_4$ nanocrystals is about 3 nm with a standard deviation of about 8%, which is depicted by the detailed size distribution analysis (inset in Figure 2b). The formation of ultrafine $ZnMn_2O_4$ nanocrystals on MWCNT may be attributed to the chemical interaction between $ZnMn_2O_4$ and the oxygen functional group sites on the moMWCNT domains.[39−41] Such a process can be confirmed by controlled experiments, in which only $ZnMn_2O_4$ microspheres with an average diameter of 1 μm could be produced under the same synthesis conditions in the absence of moMWCNT (Figure S2). It is postulated that

DOI: 10.1021/acssuschemeng.5b00434
ACS Sustainable Chem. Eng. 2015, 3, 2170−2177

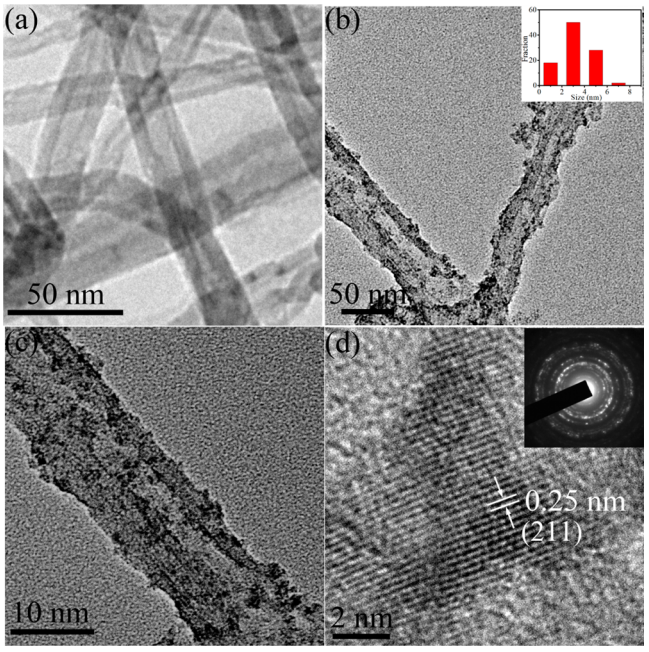

Figure 2. (a) TEM image of the moMWCNT. (b and c) TEM images of the MZMO2 (inset in b: the particle size distribution of the $ZnMn_2O_4$ nanocrystals). (d) High-resolution TEM image of the MZMO2 (inset: the corresponding selected-area electron pattern of $ZnMn_2O_4$ nanocrystals).

the $ZnMn_2O_4$ nanocrystals anchored on MWCNT would provide a large surface area for Li^+ access and effectively shorten the diffusion distance of Li^+, resulting in improved lithium storage properties.[39,43] The high-resolution TEM (HRTEM) image (Figure 2d) shows the lattice fringes with an interplanar spacing of 0.25 nm, corresponding to the distance of (211) lattice plane of spinel $ZnMn_2O_4$. The inset in Figure 2d displays that the SAED pattern of $ZnMn_2O_4$ nanocrystals possesses well-defined diffraction rings, indicating the polycrystalline nature of the resultant $ZnMn_2O_4$.[26] The existence of C, Zn, Mn and O elements in MZMO2 is proved by the STEM images (Figure 3a,b) and elemental mapping analyses (Figure 3c–f), in which the successful grafting of $ZnMn_2O_4$ nanocrystals on MWCNT is experimentally mapped out.

Figure 4a demonstrates the typical X-ray diffraction (XRD) pattern of the MZMO2. A typical tetragonal spinel structure with a space group of $I4_1/amd$ and lattice constant of $a = b = 5.720$ Å, $c = 9.245$ Å, $\alpha = \beta = \gamma = 90°$ for $ZnMn_2O_4$ can be determined. No characteristic impurity peaks are observed, indicating the high purity of $ZnMn_2O_4$ nanocrystals.[39] As shown in Figure 4b, the presence of Zn, Mn, O and C elements in MZMO2 is also confirmed by X-ray photoelectron spectroscopy (XPS). In Figure 4c, the peaks centered at binding energies (BEs) of 1021.4 and 1044.4 eV ascribe to the Zn $2p_{3/2}$ and Zn $2p_{1/2}$, respectively. The BE difference between the Zn $2p_{3/2}$ and Zn $2p_{1/2}$ peaks is 23 eV, which is in line with the Zn(II) in the $ZnMn_2O_4$ phase.[19,26,33] Figure 4d demonstrates the Mn 2p spectra at BEs of 642.4 and 654.2 eV, attributed to the Mn $2p_{3/2}$ and Mn $2p_{1/2}$, respectively. The BE separation between these two peaks is 11.8 eV, which is consistent with that of $ZnMn_2O_4$ reported previously.[26] Figure 4e depicts the high-resolution spectra of O 1s, which have been splitted into two different valence states. The peak located at 529.9 eV corresponds to the metal–oxygen bonds,[26] while the peak at 531.5 eV is attributed to C—O and C═O.[33] From the peak areas of the XPS spectra, the Mn/Zn atomic ratio is 1.87 in the MZMO2, close to the stoichiometry of the $ZnMn_2O_4$. The mass ratio of MWCNT in the MZMO2 is about 14.3 wt % determined by thermogravimertic analysis (TGA) result (Figure 4f).

The specific surface area (SSA) and porous structure are characterized by a N_2 adsorption/desorption measurement. As

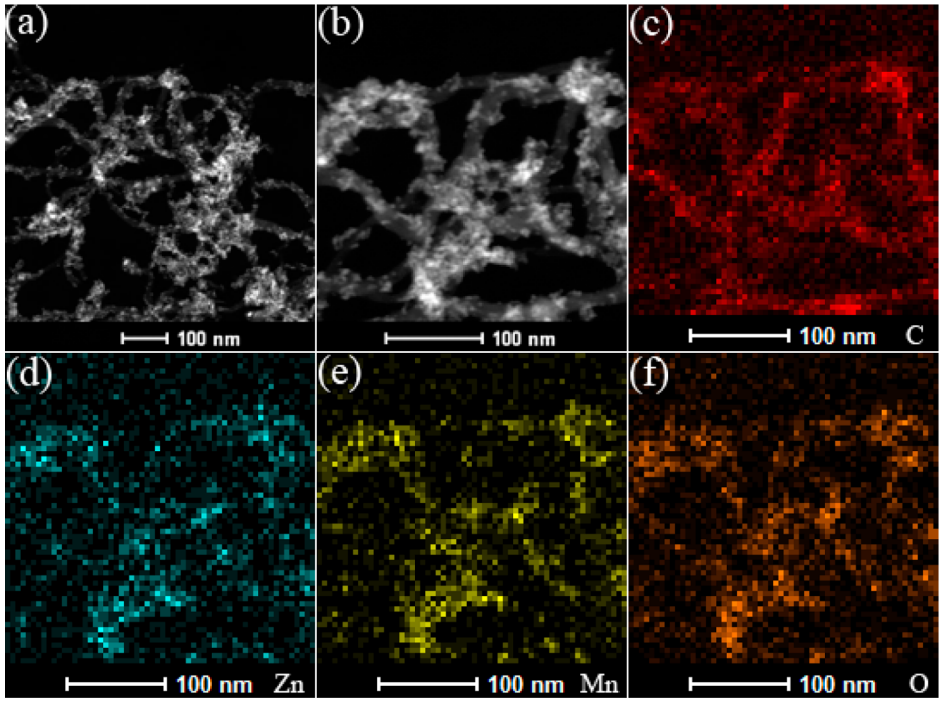

Figure 3. (a and b) STEM images of MZMO2 with corresponding elemental mapping images of (c) C, (d) Zn, (e) Mn and f (O).

DOI: 10.1021/acssuschemeng.5b00434
ACS Sustainable Chem. Eng. 2015, 3, 2170–2177

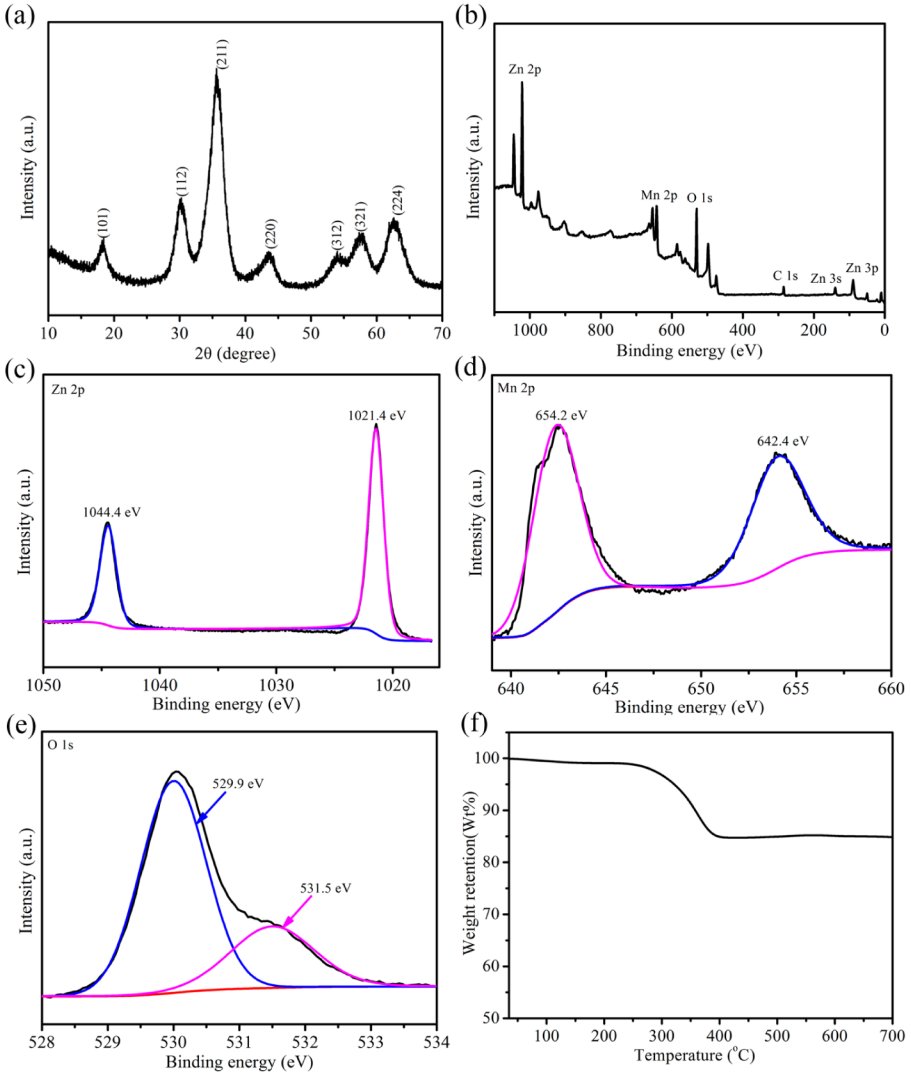

Figure 4. (a) XRD pattern of MZMO2. XPS spectra of MZMO2 (b) survey spectrum, (c) Zn 2p, (d) Mn 2p and (e) O 1s. (f) TGA of MZMO2.

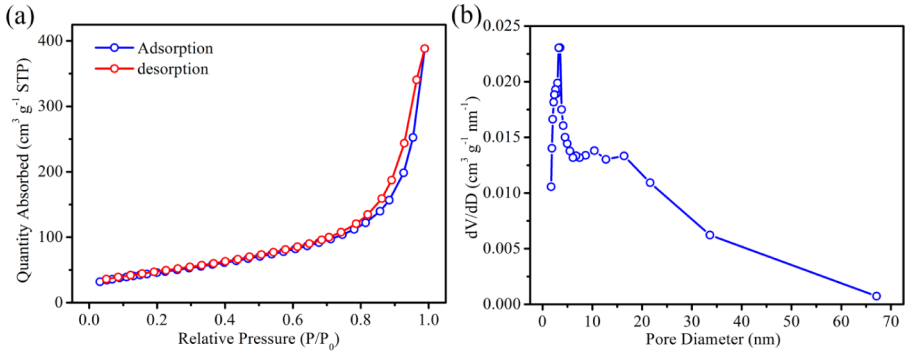

Figure 5. (a) Nitrogen adsorption/desorption isotherm and (b) pore size distribution of MZMO2.

shown in Figure 5a, the adsorption−desorption isotherm of MZMO2 exhibits typical type IV isotherm with a H_1 hysteresis loop. The Brunauer−Emmett−Teller (BET) SSA of MZMO2 calculated from the nitrogen isotherm is 165.6 m^2 g^{-1}, almost doubling the SSA of $ZnMn_2O_4$ (Supporting Information, Figure S3). In addition, an obvious hysteresis loop in the range of approximately 0.75−1.0 P/P_0 indicates that the as-prepared MZMO2 possesses mesoporous structure, which is subsequently testified by the Barrett−Joyner−Halenda (BJH) pore-size distribution (PSD) data in Figure 5b. The PSD demonstrates that the majority of the pores are in the range of 3.5−33.5 nm. The average pore size of MZMO2 is 12.4 nm. Such a mesoporous structure would greatly fast the diffusion of electrolyte to anode materials, lower the charge transfer resistance, and accommodate the volume change during discharge/charge process, endowing the hybrids excellent rate performance.[22,26]

DOI: 10.1021/acssuschemeng.5b00434
ACS Sustainable Chem. Eng. 2015, 3, 2170−2177

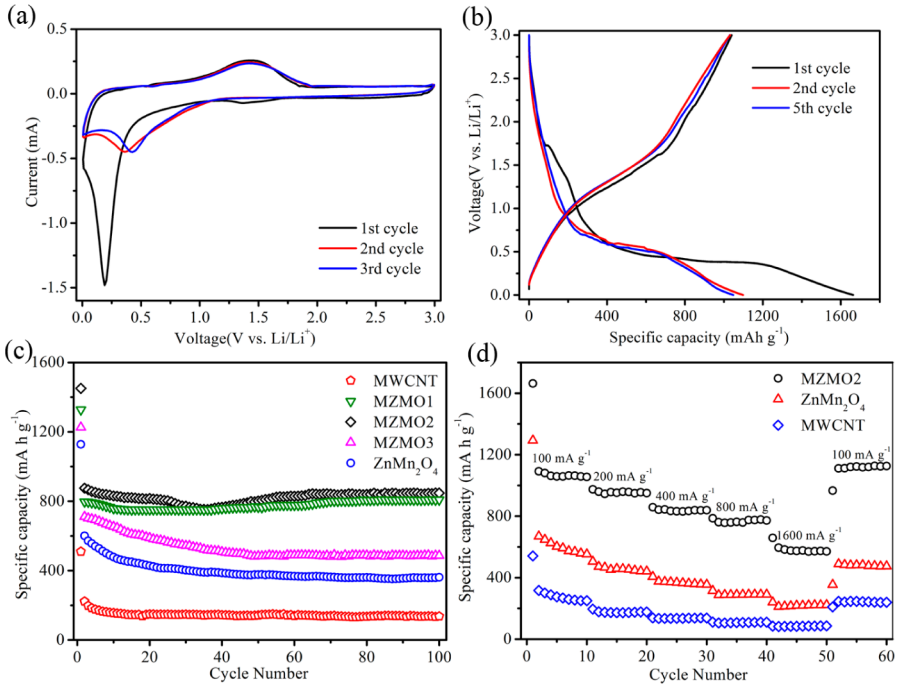

Figure 6. (a) Cycle voltammograms of MZMO2 at a scan rate of 0.1 mV s^{-1} in the voltage range of 0.01−3.0 V. (b) Galvanostatic charging/discharging curves of MZMO2 at a current density of 100 mA g^{-1} between 0.01 and 3.0 V. (c) Cycle performance of MWCNT, MZMO1, MZMO2, MZMO3 and $ZnMn_2O_4$ at a current density of 400 mA g^{-1}. (d) Rate capability of MWCNT, MZMO2 and $ZnMn_2O_4$ at different current densities of 100, 200, 400, 800 and 1600 mA g^{-1}.

The electrochemical properties of MZMO2, $ZnMn_2O_4$ and MWCNT are investigated by means of cyclic voltammetry (CV) and galvanostatic charging/discharging measurements for lithium storage. Figure 6a shows the CV curves of MZMO2 at a scan rate of 0.1 mV s^{-1} in the voltage range of 0.01−3.0 V. In the first cycle, there exists a broad reduction peak at 1.3 V, which is attributed to the reduction process of Mn^{3+} to Mn^{2+}. The reduction peak at 1.3 V vanishes in the following subsequent cycles, suggesting that Mn^{3+} will not be formed in the reverse reaction process.[39] The intensive peak at 0.20 V ascribes to the reduction of Mn^{2+} and Zn^{2+} to Mn^0 and Zn^0, which is embedded in a Li_2O matrix, followed by the formation of the Li−Zn alloy.[20,26] During the subsequent oxidation process, the broad peak at about 1.35 V could be closely associated with the reactions of Mn to MnO and Zn to ZnO along with the decomposition of Li_2O matrix.[22] In the second cycle, the intense reduction peak shifts to 0.4 V, due to the reduction of MnO and ZnO. After that, the subsequent CV curves almost overlap each other, indicating the high electrochemical reversibility.

Figure 6b shows the galvanostatic charging/discharging curves of MZMO2 at a current density of 100 mA g^{-1} between 0.01 and 3.0 V. In the process of first discharge, a well-defined long voltage plateau at about 0.45 V could be attributed to the irreversible reaction 5.[38]

$$ZnMn_2O_4 + 2Li^+ + 2e^- \rightarrow ZnO + 2MnO + Li_2O \quad (5)$$

During the following charging−discharging process, the plateau is substituted by sloping curves, owing to the reversible reaction 6.[38]

$$ZnO + 2MnO + 7Li^+ + 7e^- \leftrightarrow ZnLi + 2Mn + 3Li_2O \quad (6)$$

The initial discharge capacity and charge capacity of MZMO2 are 1663 and 1040 mAh g^{-1}, respectively, which is higher than that of MWCNT, MZMO1, MZMO3 and $ZnMn_2O_4$ (Supporting Information, Figure S5). This result indicates that the combination of $ZnMn_2O_4$ and MWCNT to form MZMO2 with proper ratio is an effective route to increase the lithium storage capability of $ZnMn_2O_4$. According to discharge/charge capacity, the Coulombic efficiency of MZMO2 is 62.5%. The 37.5% capacity loss of MZMO2 is mainly attributed to the irreversible reaction and the formation of solid electrolyte interphase (SEI) during the first charge.[14,38] The Coulombic efficiency of MZMO2 increases to 93.0% in the second cycle and stabilizes above 99% after fifth cycle, suggesting excellent reversibility of the electrode.

To evaluate further the electrochemical properties of the MZMO anode materials, stability measurements are carried out at a current density of 400 mA g^{-1} for 100 cycles in the voltage range of 0.01 to 3.0 V versus Li/Li^+ (Figure 6c). In the second cycle, the MWCNT, MZMO1, MZMO2, MZMO3 and $ZnMn_2O_4$ deliver a discharge capacity value of 222, 796, 875, 711, and 600 mA h g^{-1}, respectively. After 10 cycles, the capacity is inclined to stabilize, except for MZMO3 and pure $ZnMn_2O_4$ declining rapidly with the cycle number increasing. The capacity of MZMO2 and MZMO1 after 100 cycles can still reserve 847 and 808 mA h g^{-1}, corresponding to 96.8% and 101.5% of the second-cycle discharge capacity, respectively. For comparison, the electrodes of MZMO3 and $ZnMn_2O_4$ show poor cycle stability (Figure 6c). After 100 cycles at the same current density, the discharge capacities rapidly decrease to 486 and 361 mA h g^{-1}, resulting in capacity retentions of about 68.3% and 60.0%. The large capacity and excellent cycle performance of MZMO2 are attributed to the large specific surface area and 1D mesoporous nanostructure.[44,45] The internal pores in the MWCNT can provide good accesses for

DOI: 10.1021/acssuschemeng.5b00434
ACS Sustainable Chem. Eng. 2015, 3, 2170−2177

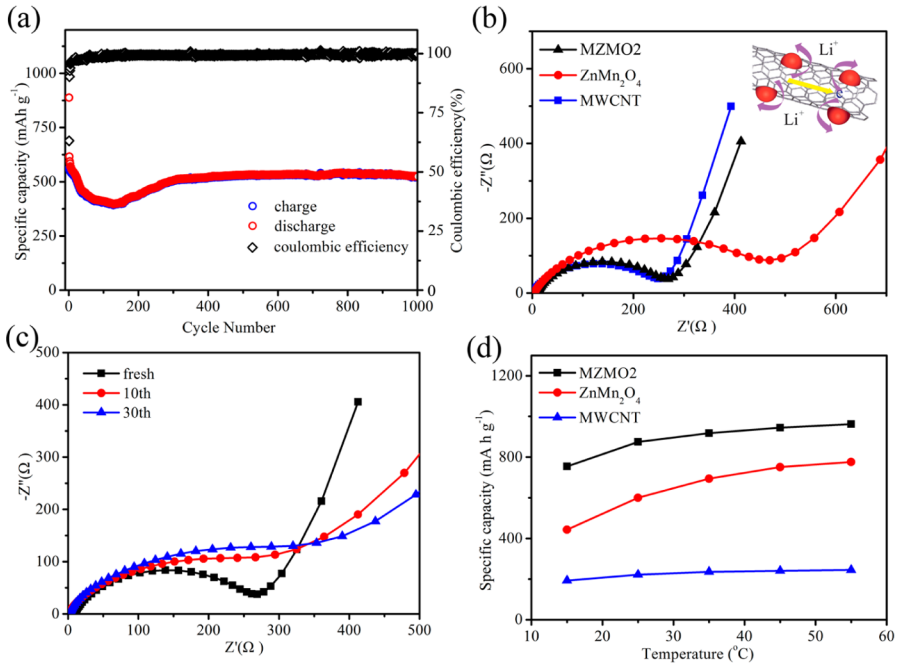

Figure 7. (a) Cycle performance and Coulombic efficiency of MZMO2 at a current density of 1600 mA g^{-1} for 1000 cycles. (b) Electrochemical impedance spectra (EIS) of MWCNT, MZMO2 and $ZnMn_2O_4$ before cycle (inset: schematic of the lithium storage advantage of MZMO2). (c) EIS of MZMO2 at different cycles. (d) Temperature-dependent specific discharge capacities of MWCNT, MZMO2 and $ZnMn_2O_4$ at a specific current density of 400 mA g^{-1}.

the electrolyte to the electrode surface. Large surface area facilitates charge transfer and shortens Li^+ diffusion distance.[46,47] Furthermore, strong interaction between $ZnMn_2O_4$ nanocrystals and flexible MWCNT could maintain the integrity, and restrain volume change of the anode material during the repeated Li^+ insertion/extraction,[41,48] thus leading to high capacity and good cycle stability.

The rate properties of MZMO2, pure $ZnMn_2O_4$ and MWCNT are shown in Figure 6d. Pure $ZnMn_2O_4$ delivers a specific capacity of nearly 668 mA h g^{-1} at a current density of 100 mA g^{-1}, but only 239 mA h g^{-1} at 1600 mA g^{-1}. In comparison, MZMO2 electrode demonstrates remarkable rate capability as expected, which gives specific capacities of 1092, 974, 858, 786 and 595 mA h g^{-1} at the current densities of 100, 200, 400, 800 and 1600 mA g^{-1}. Even at a high current density of 1600 mA g^{-1}, the capacity is still much higher than the theoretical capacity of graphite (372 mA h g^{-1}). Notably, the capacity could resume to a high value of 1111 mA h g^{-1}, when the current density is returned from 1600 to 100 mA g^{-1}, indicating good reversibility of the electrode material. Remarkably, the excellent rate capability makes the MZMO2 a more promising electrode compared with previously reported $ZnMn_2O_4$-based electrodes (Supporting Information, Table S1).

The long-term cyclability measurement of the as-prepared MZMO2 is conducted as an anode for LIBs at a current density of 1600 mA g^{-1} up to 1000 cycles. As shown in Figure 7a, the discharge capacity is 527 mA h g^{-1} after 1000 cycles, along with the Coulombic efficiency close to 100%. It is noteworthy that the capacity gradually decreases to 398 mA h g^{-1} after about 130 cycles. Interesting, the capacity begins to increase during the subsequent 180 cycles, and then keeps a value as high as 527 mA h g^{-1} after 1000 cycles. This phenomenon is consistent with previous reports and could be attributed to the reversible growth of the electro-chemistry active polymeric gel-like film by the kinetically activated electrolyte degradation.[14,39,49] To the best of our knowledge, the cycle stability of MZMO2 electrode is better than most of documents reported about $ZnMn_2O_4$-based anodes (Supporting Information, Table S1).

To clarify the excellent lithium storage properties of MZMO2, electrochemical impedance spectra (EIS) are carried out in the frequency range from 10 mHz to 100 kHz (Figure 7b). In the high to medium frequency region, the diameter of the semicircle for MZMO2 is much smaller than that of pure $ZnMn_2O_4$, indicating the lower contact and charge-transfer impedances.[14,38] In the low frequency region, the larger slope of the hybrid in comparison with pure $ZnMn_2O_4$ demonstrates the faster Li^+-ion diffusion behavior of MZMO2 electrode.[14] As shown in Figure 7c, there is obvious increase of impedance for MZMO2 after 10 cycles, estimated from the depressed semicircles compared to the fresh cell. The increase in resistance is approximately owing to the formation of a SEI. From 10 to 30 cycles, the resistance has no significant increase. According to the depressed semicircles of MZMO2 (Figure 7c) and $ZnMn_2O_4$ (Figure S6) electrodes, the resistance of MZMO2 is much lower than that of $ZnMn_2O_4$ at different cycles, indicating a stable structure and excellent electrochemical properties of the nanocomposite.

Figure 7d depicts temperature-dependent specific discharge capacities of MWCNT, MZMO2 and $ZnMn_2O_4$ at a specific current density of 400 mA g^{-1}. The specific discharge capacity of MZMO2 is 962 mA h g^{-1} at 55 °C. As reducing the temperature to 15 °C, there is still a specific capacity of 754 mA h g^{-1} reserved, corresponding to only 21.6% capacity decrease. Yet, the specific capacity of $ZnMn_2O_4$ is obviously decreased by 42.9% in the same temperature range from 55 to 15 °C.

The outstanding electrochemical performance of MZMO2 originates from the chemically integrated 1D mesoporous nanostructure. The MWCNT severs as a conductive layer to ensure the rapid charge transfer between $ZnMn_2O_4$ and the

DOI: 10.1021/acssuschemeng.5b00434
ACS Sustainable Chem. Eng. 2015, 3, 2170−2177

current collector, increasing the reaction kinetics.[35,50] The ultrafine $ZnMn_2O_4$ nanocrystals can provide more electrochemically active sites for Li^+ storage, resulting in the high reversible capacity.[39] Moreover, the 1D mesoporous nanostructure of MZMO2 not only allows sufficient infiltration of electrolyte to provide rapid diffusion channels for Li^+ shuttling, leading to excellent rate capability, but also accommodates volume change during cycling, resulting in good cycle life.[39] More significantly, the covalent coupled interaction and synergic effect (inset in Figure 7b) between MWCNT and $ZnMn_2O_4$ could further restrain the volume expansion/contraction and aggregation of $ZnMn_2O_4$ nanocrystals in the process of discharge/charge, which are consequently responsible for the high rate capability and ultralong-life up to 1000 cycles.[39,48]

CONCLUSIONS

In summary, chemically integrated 1D MWCNT/$ZnMn_2O_4$ (MZMO) with mesoporous structure has been synthesized through a cost-effective two-step strategy involving a simple polyol process and a facile thermal annealing treatment in air. The MZMO2 anode exhibits a high reversible lithium storage capacity of 847 mA h g^{-1} after 100 cycles at a current density of 400 mA g^{-1}, as well as excellent rate capability and ultralong life up to 1000 cycles, due to the well-defined structure features including strongly coupled interaction and synergic effect between $ZnMn_2O_4$ nanocrystals and MWCNT. Thus, it can be predicted that this hybrid could be a promising candidate material as a high-performance and environmental friendly anode for lithium-ion batteries.

ASSOCIATED CONTENT

Supporting Information

The Supporting Information is available free of charge on the ACS Publications website at DOI: 10.1021/acssuschemeng.5b00434.

Experimental details, ATR-IR spectra of MWCNT and moMWCNT, SEM images of $ZnMn_2O_4$ microspheres, and electrochemical characterizations (PDF).

AUTHOR INFORMATION

Corresponding Author

*W. Yao. Tel.: +(86)-515-88298872. Fax: +(86)-515-88298872. E-mail: xiaoniu1981@126.com.

Notes

The authors declare no competing financial interest.

ACKNOWLEDGMENTS

This work was supported by the Natural Science Foundation of Jiangsu Province (BK20140473 and BK20131220), Scientific Research Foundation for Returned Scholars, Ministry of Education of China and Research fund of Yancheng Institute of Technology (KJC2013006).

REFERENCES

(1) Liu, N.; Lu, Z.; Zhao, J.; McDowell, M. T.; Lee, H.; Zhao, W.; Cui, Y. A pomegranate-inspired nanoscale design for large-volume-change lithium battery anodes. *Nat. Nanotechnol.* **2014**, *9*, 187−192.

(2) Wang, K.; Li, X.; Chen, J. Surface and interface engineering of electrode materials for lithium-ion batteries. *Adv. Mater.* **2015**, *27*, 527−545.

(3) Wang, H.; Dai, H. Strongly coupled inorganic-nano-carbon hybrid materials for energy storage. *Chem. Soc. Rev.* **2013**, *42*, 3088−3113.

(4) de las Casas, C.; Li, W. A review of application of carbon nanotubes for lithium ion battery anode material. *J. Power Sources* **2012**, *208*, 74−85.

(5) Goodenough, J. B.; Park, K. The Li-ion rechargeable battery: a perspective. *J. Am. Chem. Soc.* **2013**, *135*, 1167−1176.

(6) Gao, G.; Wu, H. B.; Dong, B.; Ding, S.; Lou, X. Growth of ultrathin $ZnCo_2O_4$ nanosheets on reduced graphene oxide with enhanced lithium storage properties. *Adv. Sci.* **2015**, *2*, 1400014.

(7) Xiao, X.; Liu, X.; Zhao, H.; Chen, D.; Liu, F.; Xiang, J.; Hu, Z.; Li, Y. Facile shape control of Co_3O_4 and the effect of the crystal plane on electrochemical performance. *Adv. Mater.* **2012**, *24*, 5762−5766.

(8) Jiang, H.; Hu, Y.; Guo, S.; Yan, C.; Lee, P. S.; Li, C. Rational design of MnO/carbon nanopeapods with internal void space for high-rate and long-life Li-ion batteries. *ACS Nano* **2014**, *8*, 6038−6046.

(9) Han, F.; Li, D.; Li, W.; Lei, C.; Sun, Q.; Lu, A. Nanoengineered polypyrrole-coated Fe_2O_3@C multifunctional composites with an improved cycle stability as lithium-ion anodes. *Adv. Funct. Mater.* **2013**, *23*, 1692−1700.

(10) Wang, J.; Du, N.; Zhang, H.; Yu, J.; Yang, D. Large-scale synthesis of SnO_2 nanotube arrays as high-performance anode materials of Li-ion batteries. *J. Phys. Chem. C* **2011**, *115*, 11302−11305.

(11) Gu, X.; Yue, J.; Chen, L.; Liu, S.; Xu, H.; Yang, J.; Qian, Y.; Zhao, X. Coaxial MnO/N-doped carbon nanorods for advanced lithium-ion battery anodes. *J. Mater. Chem. A* **2015**, *3*, 1037−1041.

(12) Wang, S.; Pu, J.; Tong, Y.; Cheng, Y.; Gao, Y.; Wang, Z. $ZnCo_2O_4$ nanowire arrays grown on nickel foam for high-performance pseudocapacitors. *J. Mater. Chem. A* **2014**, *2*, 5434−5440.

(13) Choi, S. H.; Kang, Y. C. Yolk-shell, hollow, and single-crystalline $ZnCo_2O_4$ powders: preparation using a simple one-pot process and application in lithium-ion batteries. *ChemSusChem* **2013**, *6*, 2111−2116.

(14) Bai, J.; Li, X.; Liu, G.; Qian, Y.; Xiong, S. Unusual formation of $ZnCo_2O_4$ 3D hierarchical twin microspheres as a high-rate and ultralong-life lithium-ion battery anode material. *Adv. Funct. Mater.* **2014**, *24*, 3012−3020.

(15) Guo, H.; Liu, L.; Li, T.; Chen, W.; Liu, J.; Guo, Y.; Guo, Y. Accurate hierarchical control of hollow crossed $NiCo_2O_4$ nanocubes for superior lithium storage. *Nanoscale* **2014**, *6*, 5491−5497.

(16) Deng, Y.; Tang, S.; Zhang, Q.; Shi, Z.; Zhang, L.; Zhan, S.; Chen, G. Controllable synthesis of spinel nano-$ZnMn_2O_4$ via a single source precursor route and its high capacity retention as anode material for lithium ion batteries. *J. Mater. Chem.* **2011**, *21*, 11987−11995.

(17) Teh, P. F.; Sharma, Y.; Pramana, S. S.; Srinivasan, M. Nanoweb anodes composed of one-dimensional, high aspect ratio, size tunable electrospun $ZnFe_2O_4$ nanofibers for lithium batteries. *J. Mater. Chem.* **2011**, *21*, 14999−15008.

(18) Xing, Z.; Ju, Z.; Yang, J.; Xu, H.; Qian, Y. One-step hydrothermal synthesis of $ZnFe_2O_4$ nano-octahedrons as a high capacity anode material for Li-ion batteries. *Nano Res.* **2012**, *5*, 477−485.

(19) Kim, J. G.; Lee, S. H.; Kim, Y.; Kim, W. B. Fabrication of free-standing $ZnMn_2O_4$ mesoscale tubular arrays for lithium-ion anodes with highly reversible lithium storage properties. *ACS Appl. Mater. Interfaces* **2013**, *5*, 11321−11328.

(20) Bai, Z.; Fan, N.; Sun, C.; Ju, Z.; Guo, C.; Yang, J.; Qian, Y. Facile synthesis of loaf-like $ZnMn_2O_4$ nanorods and their excellent performance in Li-ion batteries. *Nanoscale* **2013**, *5*, 2442−2447.

(21) Li, G.; Wang, Y.; Yang, L.; Ma, W.; Wang, M. In situ synthesis of $ZnMn_2O_4$-ZnO-C and $ZnMn_2O_4$-C nanohybrids as high performance lithium-ion battery anodes. *Eur. J. Inorg. Chem.* **2014**, *2014*, 845−851.

(22) Wang, N.; Ma, X.; Xu, H.; Chen, L.; Yue, J.; Niu, F.; Yang, J.; Qian, Y. Porous $ZnMn_2O_4$ microspheres as a promising anode material for advanced lithium-ion batteries. *Nano Energy* **2014**, *6*, 193−199.

DOI: 10.1021/acssuschemeng.5b00434
ACS Sustainable Chem. Eng. 2015, 3, 2170−2177

(23) Xiao, L.; Yang, Y.; Yin, J.; Li, Q.; Zhang, L. Low temperature synthesis of flower-like $ZnMn_2O_4$ superstructures with enhanced electrochemical lithium storage. *J. Power Sources* **2009**, *194*, 1089−1093.
(24) Song, M. S.; Cho, Y. J.; Yoon, D. Y.; Nahm, S.; Oh, S. H.; Woo, K.; Ko, J. M.; Cho, W. I. Solvothermal synthesis of $ZnMn_2O_4$ as an anode material in lithium ion battery. *Electrochim. Acta* **2014**, *137*, 266−272.
(25) Courtel, F. M.; Abu-Lebdeh, Y.; Davidson, I. J. $ZnMn_2O_4$ nanoparticles synthesized by a hydrothermal method as an anode material for Li-ion batteries. *Electrochim. Acta* **2012**, *71*, 123−127.
(26) Yuan, C.; Zhang, L.; Hou, L.; Zhou, L.; Pang, G.; Lian, L. Scalable room-temperature synthesis of mesoporous nanocrystalline $ZnMn_2O_4$ with enhanced lithium storage properties for lithium-ion batteries. *Chem. - Eur. J.* **2015**, *21*, 1262−1268.
(27) Yang, Y.; Zhao, Y.; Xiao, L.; Zhang, L. Nanocrystalline $ZnMn_2O_4$ as a novel lithium-storage material. *Electrochem. Commun.* **2008**, *10*, 1117−1120.
(28) Zhou, L.; Wu, H. B.; Zhu, T.; Lou, X. W. Facile preparation of $ZnMn_2O_4$ hollow microspheres as high-capacity anodes for lithium-ion batteries. *J. Mater. Chem.* **2012**, *22*, 827−829.
(29) Liu, Y.; Bai, J.; Ma, X.; Li, J.; Xiong, S. Formation of quasi-mesocrystal $ZnMn_2O_4$ twin microspheres via an oriented attachment for lithium-ion batteries. *J. Mater. Chem. A* **2014**, *2*, 14236−14244.
(30) Zhang, G.; Yu, L.; Wu, H. B.; Hoster, H. E.; Lou, X. W. Formation of $ZnMn_2O_4$ ball-in-ball hollow microspheres as a high-performance anode for lithium-ion batteries. *Adv. Mater.* **2012**, *24*, 4609−4613.
(31) Chen, X.; Qie, L.; Zhang, L.; Zhang, W.; Huang, Y. Self-templated synthesis of hollow porous submicron $ZnMn_2O_4$ sphere as anode for lithium-ion batteries. *J. Alloys Compd.* **2013**, *559*, 5−10.
(32) Kim, S.; Lee, H.; Muralidharan, P.; Seo, D.; Yoon, W.; Kim, D. K.; Kang, K. Electrochemical performance and ex situ analysis of $ZnMn_2O_4$ nanowires as anode materials for lithium rechargeable batteries. *Nano Res.* **2011**, *4*, 505−510.
(33) Yuan, C.; Zhang, L.; Zhu, S.; Cao, H.; Lin, J.; Hou, L. Heterostructured core-shell $ZnMn_2O_4$ nanosheets@carbon nanotubes' coaxial nanocables: a competitive anode towards high-performance Li-ion batteries. *Nanotechnology* **2015**, *26*, 145401.
(34) Xu, X.; Dong, B.; Ding, S.; Xiao, C.; Yu, D. Hierarchical $NiCoO_2$ nanosheets supported on amorphous carbon nanotubes for high-capacity lithium-ion batteries with a long cycle life. *J. Mater. Chem. A* **2014**, *2*, 13069−13074.
(35) Yin, L.; Zhang, Z.; Li, Z.; Hao, F.; Li, Q.; Wang, C.; Fan, R.; Qi, Y. Spinel $ZnMn_2O_4$ nanocrystal-anchored 3D hierarchical carbon aerogel hybrids as anode materials for lithium ion batteries. *Adv. Funct. Mater.* **2014**, *24*, 4176−4185.
(36) Jia, X.; Chen, Z.; Suwarnasarn, A.; Rice, L.; Wang, X.; Sohn, H.; Zhang, Q.; Wu, B. M.; Wei, F.; Lu, Y. High-performance flexible lithium-ion electrodes based on robust network architecture. *Energy Environ. Sci.* **2012**, *5*, 6845−6849.
(37) Huang, X.; Wang, R.; Xu, D.; Wang, Z.; Wang, H.; Xu, J.; Wu, Z.; Liu, Q.; Zhang, Y.; Zhang, X. Homogeneous CoO on graphene for binder-free and ultralong-life lithium ion batteries. *Adv. Funct. Mater.* **2013**, *23*, 4345−4353.
(38) Zheng, Z.; Cheng, Y.; Yan, X.; Wang, R.; Zhang, P. Enhanced electrochemical properties of grapheme-wrapped $ZnMn_2O_4$ nanorods for lithium-ion batteries. *J. Mater. Chem. A* **2014**, *2*, 149−154.
(39) Xiong, P.; Liu, B.; Teran, V.; Zhao, Y.; Peng, L.; Wang, X.; Yu, G. Chemically integrated two-dimensional hybrid zinc manganate/graphene nanosheets with enhanced lithium storage capability. *ACS Nano* **2014**, *8*, 8610−8616.
(40) Wang, H.; Liang, Y.; Gong, M.; Li, Y.; Chang, W.; Mefford, T.; Zhou, J.; Wang, J.; Regier, T.; Wei, F.; Dai, H. An ultrafast nickel-iron battery from strongly coupled inorganic nanoparticle/nanocarbon hybrid materials. *Nat. Commun.* **2012**, *3*, 917.
(41) Liang, Y.; Wang, H.; Diao, P.; Chang, W.; Hong, G.; Li, Y.; Gong, M.; Xie, L.; Zhou, J.; Wang, J.; Regier, T. Z.; Wei, F.; Dai, H. Oxygen reduction electrocatalyst based on strongly coupled cobalt oxide nanocrystals and carbon nanotubes. *J. Am. Chem. Soc.* **2012**, *134*, 15849−15857.
(42) Zhou, H.; Yao, W.; Li, G.; Wang, J.; Lu, Y. Graphene/ poly(3,4-ethylenedioxythiophene) hydrogel with excellent mechanical performance and high conductivity. *Carbon* **2013**, *59*, 495−502.
(43) Zhang, G.; Xia, B. Y.; Wang, X.; Lou, X. W. Strongly coupled $NiCo_2O_4$-rGO as a methanol-tolerant electrocatalyst for oxygen reduction reaction. *Adv. Mater.* **2014**, *26*, 2408−2412.
(44) Sun, Y.; Hu, X.; Luo, W.; Xia, F.; Huang, Y. Reconstruction of conformal nanoscale MnO on graphene as a high-capacity and long-life anode material for lithium ion batteries. *Adv. Funct. Mater.* **2013**, *23*, 2436−2444.
(45) Shin, W. H.; Jeong, H. M.; Kim, B. G.; Kang, J. K.; Choi, J. W. Nitrogen-doped multiwall carbon nanotubes for lithium storage with extremely high capacity. *Nano Lett.* **2012**, *12*, 2283−2288.
(46) Vu, A.; Qian, Y.; Stein, A. Porous electrode materials for lithium-ion batteries-how to prepare them and what makes them special. *Adv. Energy Mater.* **2012**, *2*, 1056−1085.
(47) Li, Y.; Fu, Z.; Su, B. Hierarchically structured porous materials for energy conversion and storage. *Adv. Funct. Mater.* **2012**, *22*, 4634−4667.
(48) Zhang, G.; Wu, H. B.; Hoster, H. E.; Lou, X. W. Strongly coupled carbon nanofiber-metal oxide coaxial nanocables with enhanced lithium storage properties. *Energy Environ. Sci.* **2014**, *7*, 302−305.
(49) Zhou, G.; Wang, D.; Li, F.; Zhang, L.; Li, N.; Wu, Z.; Wen, L.; Lu, G.; Cheng, H. Graphene-wrapped Fe_3O_4 anode material with improved reversible capacity and cyclic stability for lithium ion batteries. *Chem. Mater.* **2010**, *22*, 5306−5313.
(50) Wu, Z.; Ren, W.; Wen, L.; Gao, L.; Zhao, J.; Chen, Z.; Zhou, G.; Li, F.; Cheng, H. Graphene anchored with Co_3O_4 nanoparticles as anode of lithium ion batteries with enhanced reversible capacity and cyclic performance. *ACS Nano* **2010**, *4*, 3187−3194.

DOI: 10.1021/acssuschemeng.5b00434
ACS Sustainable Chem. Eng. 2015, 3, 2170−2177